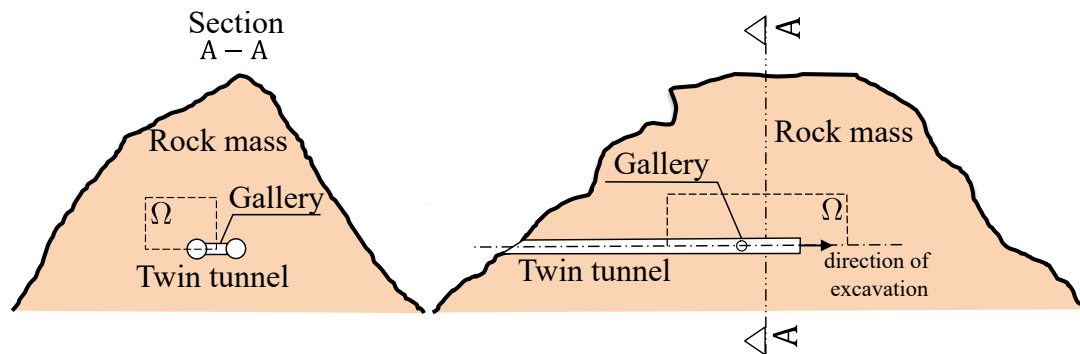


Graphical Abstract

Numerical analysis of the twin tunnels with transverse galleries using plastic and viscous constitutive models for rockmass and lining

Quevedo, F. P. M., Colombo, C. A. M. M., Bernaud, D., Maghous, S.



Highlights

Numerical analysis of the twin tunnels with transverse galleries using plastic and viscous constitutive models for rockmass and lining

Quevedo, F. P. M.,Colombo, C. A. M. M.,Bernaud, D.,Maghous, S.

- Qualquer coisa 1
- Qualquer coisa 2
- Qualquer coisa 3

Numerical analysis of the twin tunnels with transverse galleries using plastic and viscous constitutive models for rockmass and lining

Quevedo, F. P. M.^{a,*}, Colombo, C. A. M. M.^a, Bernaud, D.^a and Maghous, S.^a

^aFederal University of Rio Grande do Sul, Av. Osvaldo Aranha, 99, Porto Alegre, 90.035-190, RS, Brazil

ARTICLE INFO

Keywords:

twin tunnels
transverse gallery
constitutive models
finite element method

ABSTRACT

This paper aims to demonstrate the long-term implications of the rheological constitutive behavior of rock mass and concrete lining in the convergence profile of the twin tunnels with transverse galleries using a three-dimensional numerical analysis based on the finite-element method. Various constitutive models are considered for the rock mass, including elastic, elastoplastic, viscoplastic, and elastoplastic-viscoplastic. The definition of plasticity incorporates a Drucker-Prager yield surface and an associated flow rule without hardening or softening. Viscoplasticity is based on the Perzyna model, also using a Drucker-Prager flow surface. For the lining, elastic and viscoelastic constitutive models are adopted. The viscoelastic behavior is defined by a Generalized Kelvin rheological model, formulated based on the Solidification Theory of Bazand and Prassanann, with parameters given by CEB-FIP MC90 formulations. The deactivation-activation method simulate the excavation process. The numerical model is verified using comparisons with analytical solutions in elasticity and elastoplasticity for twin tunnels without a gallery developed by other authors. The mutual interaction between the longitudinal tunnels through parametric analyses is investigated, emphasizing the impact of the concrete lining stiffness on tunnel convergences. The interaction is particularly significant for longitudinal tunnels, especially when they are spaced at four radius. With a transverse gallery and considering the lining, we observe a highly localized influence in twin tunnels, extending up to four radius on each side of the gallery axis. Comparisons of convergence reveal that the viscous effects of the rock mass and the lining significantly influence the peak convergence within the intersection zone, resulting in differences of approximately 10% in convergence values.


1. Introduction


Many design methods often focus on single tunnels, but twin tunnels are a common occurrence. The interaction between tunnels can be significant, especially when the spacing between them is minimal. Additionally, many twin tunnels incorporate transverse galleries, introducing a localized effect on displacements and stresses. Also, the rheological behavior of the rockmass and lining plays a crucial role in how stress and displacements fields evolve over time. Some recent studies on deep twin tunnels can be found at [19, 6, 11, 7, 8, 12, 9, 10].

Chortis and Kavvadas [7] considered the calculation of the axial forces acting on the primary support in the intersection zone before, during, and after the construction of a transverse tunnel linking twin tunnels. The results of the analysis indicated that the zone of influence extends approximately two diameters from the main tunnel to each side from the center of the intersection and that the interaction effects are practically eliminated when they exceed this delimited zone of influence.

In another study, Chortis and Kavvadas [8] carried out parametric 3D finite element analyses to verify the interaction between deep twin tunnel, with circular and non-circular section, supported by a shotcrete lining, considering the rock mass with linear elastic behavior, perfectly plastic, with Mohr-Coulumb failure criteria, and the elastic linear lining. The study investigates the axial forces that develop in the primary lining of the twin tunnels as

*Corresponding author.

 motta.quevedo@ufrgs.br (Q.F.P. M.); carlos.colombo@ufrgs.br (C.C.A.M. M.); denise.bernaud@ufrgs.br (B. D.); samir.maghous@ufrgs.br (M. S.)

 <https://www.researchgate.net/profile/Felipe-Pinto-Da-Motta-Quevedo> (Q.F.P. M.); <http://lattes.cnpq.br/4919388217690564> (C.C.A.M. M.); <http://lattes.cnpq.br/2809615143819128> (B. D.); <http://lattes.cnpq.br/6305244914209829> (M. S.)

ORCID(s): 0000-0003-4171-1696 (Q.F.P. M.); 0000-0000-0000-0000 (C.C.A.M. M.); 0000-0001-6365-3269 (B. D.); 0000-0002-1123-3411 (M. S.)

a function of the main geometric and geomaterial parameters, but without considering the potential time-dependent deformations (creep effect) that occur in some types of rock masses.

Chen et al. [6], through analytical solutions in elasticity using complex variables, Fourier transformation, and the alternating Schwarz method, demonstrate that the mutual interaction between twin tunnels disappears if the spacing between the tunnels is greater than six times the tunnel radius. The lining effectively reduces the stress concentration, especially at high lateral stress coefficients.

Guo et al. [12] develop an elastic analytical solution for the stress field around twin circular tunnels with hydrostatic pressure using the complex variable and the superposition principle. They found that stress concentration in tunnel wall increased as the distance between the parallel tunnels and the pressure on the support decreased.

Ma et al. [13] proposed an analytical method, verified by a numerical solution using FLAC3D software for determining the plasticization zones around deep circular twin tunnels without linings, restricting themselves where there is no overlap between the two plastic zones. In this case, they adopted the perfectly plastic elastic constitutive model for the homogeneous and isotropic mass, with the Mohr-Coulomb criterion for the flow surface. They also carried out parametric studies to understand the influence of the distance between the twin tunnels, cohesion, the angle of internal friction, and the vertical and horizontal stresses acting on the shape and depth of the plastic zones. They recognizing the plastic zone around the tunnel provides a relevant theoretical basis for defining and designing the support. In addition, they mention that an excessive plastic zone significantly affects the stability and functionality of a tunnel. Therefore, the delimitation of the plastic zone around tunnels is of great importance for the development of projects.

Using parametric three-dimensional numerical analyses, Chortis and Kavvadas [9, 10] investigated the effect of building a transverse tunnel that intersected deep twin tunnels perpendicularly, focusing the study on the axial forces and the circumferential and longitudinal bending moments acting on the primary support of the intersection regions, respectively. According to the authors, the potential interaction between deep twin tunnels lined with shotcrete must be taken into account, especially when the distance between them is less than or equal to twice their diameter.

According to Fortsakis [11], in a realistic construction context, twin tunnels are excavated and supported with a delay, so that the second tunnel is usually built after the first one has advanced enough to maintain a longitudinal separation distance between the faces. The advance of the subsequent tunnel mobilizes the redistribution of stresses and deformations in the zone between the tunnels, resulting in additional loading of the preceding tunnel.

As for transverse tunnels, these are generally built far enough behind the advanced face of the main tunnel to ensure that their excavation has virtually no effect during the construction of the junction tunnel [7]. The interaction at the intersection, between the main tunnel and the transverse tunnel, significantly modifies the stress state of the primary support and that of the surrounding rock mass in these areas, compared to that of the singular tunnel, making three-dimensional finite element analyses essential for developing a realistic and safe design for tunnel junctions [19].

During the construction of the transverse tunnel, the surrounding rock mass is subjected to a redistribution of stresses, causing an additional load on the main tunnel, precisely in the intersection zone. If these additional loads exceed the load capacity of the primary support of the main tunnel, a potentially unstable region can develop, leading to failure, especially in adverse geotechnical conditions [7].

The long-term effect has been investigated for single tunnels, but little research has been done on twin tunnels, especially with a gallery. Therefore, in this work, the aim is to investigate the influence of the distance between the tunnels and the effect that the gallery has on the long-term convergence profile of deep-lined twin tunnels, considering various constitutive laws for the rock mass and the lining.

2. Fundamental assumptions

Despite the generality of the models, we employ some delimitations in this work:

- (a) It is assumed only deep tunnels, neglecting surface influences such as deformations caused by surface loads and settlements arising from the excavation process;
- (b) Although the inherent complexity of the rock mass's behavior, is influenced by spatially varying properties, this study opts for a simplified representation: a homogeneous and isotropic medium. While the rock mass may exhibit discontinuities, we simplify its overall behavior by treating it as a continuous medium. Consequently, the rock mass is considered single-phase and phenomenologically modeled using an elastoplastic-viscoplastic rheological law to capture instantaneous and long-term responses. This approach excludes considerations of other factors, such as temperature gradients, water flow, and pore mechanics;

- (c) Despite the complexity of the internal stress state of a massif, due, for example, to the discontinuities, anisotropy, and heterogeneity of the materials, equal vertical and horizontal stresses will be used, thus dealing with a geostatic-hydrostatic initial stress state.
- (d) It is common to design twin tunnels with a time lag between the excavation fronts. In this work, we will perform synchronous excavation, using symmetry conditions to minimize computer processing time.
- (e) In contrast to the variable conditions present in tunnel construction, where the excavation speed and lining installation fluctuate during the construction process, we adopt a constant speed for full, flat, and vertical excavation with homogeneous concrete lining with constant thickness. It's considered a constant humidity and temperature in the concrete lining.
- (f) We will not consider dynamic excitations (involving earthquakes and explosions, for example) and inertial terms (density and acceleration). In other words, the evolution of deformations occurs in a quasi-static manner. We also adopt the hypothesis of small perturbations.

3. Constitutive Model of the Rock Material

An elastoplastic-viscoplastic constitutive model was implemented in ANSYS using the UPF/USERMAT customization tool [1] to simulate rock mass. This model concern a serial association of the plastic and viscoplastic constitutive models, i.e., the total strain $\dot{\epsilon} = \dot{\epsilon}^e + \dot{\epsilon}^p + \dot{\epsilon}^{vp}$, which leads to the following linear constitutive relationship:

$$\dot{\sigma} = \mathbf{D} : \dot{\epsilon}^e = \mathbf{D} : (\dot{\epsilon} - \dot{\epsilon}^p - \dot{\epsilon}^{vp}), \quad (1)$$

where $\dot{\epsilon}^e$, $\dot{\epsilon}^p$ and $\dot{\epsilon}^{vp}$, represent the elastic, plastic and viscoplastic strain rate, respectively and \mathbf{D} denote the fourth-order isotropic elastic linear constitutive tensor. The one-dimensional representation in Fig. 1 shows this association. In this

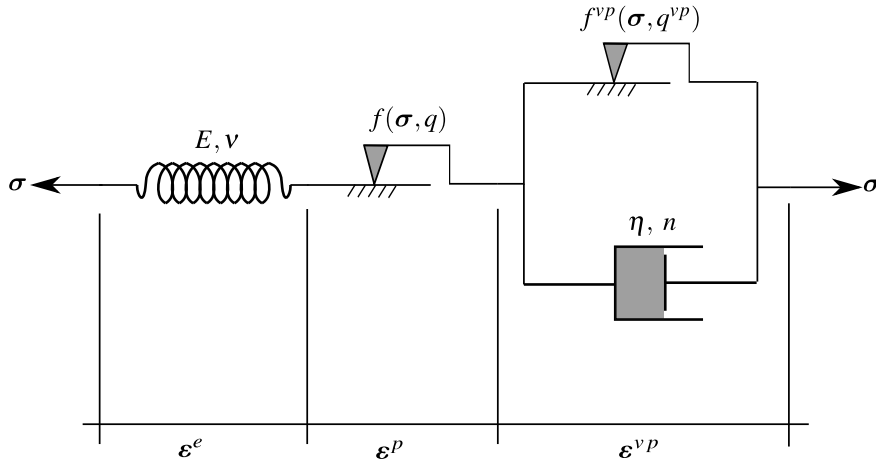


Figure 1: Rheological representation of the elastoplastic-viscoplastic model.

model is used a Drucker-Prager plastic flow surface given by

$$f(\sigma, q) = f(I_1, J_2, q) = \beta_1 I_1 + \beta_2 \sqrt{J_2} - q(\alpha), \quad (2)$$

which I_1 is the first invariant of the stress tensor, J_2 the second invariant of the deviator tensor and β_1, β_2 and $q(\alpha)$ are strength parameters related to the friction angle ϕ and cohesion $c(\alpha)$, respectively. In the present model Drucker-Prager surface been inner of the Mohr-Coulomb surface [4], that is,

$$\beta_1 = \frac{(k-1)}{3}, \quad \beta_2 = \frac{(2k+1)}{\sqrt{3}}, \quad q(\alpha) = 2\sqrt{k} c(\alpha), \quad (3)$$

where $k = (1 + \sin \phi)/(1 - \sin \phi)$. The internal variable α is the equivalent plastic strain $\bar{\epsilon}^p$ used to simulate strain hardening/softening phenomena. However, for this study, we adopt perfect plasticity, meaning that c is a constant. For

the viscoplasticity surface f^{vp} the same surface is employed, but with ϕ^{vp} in β_1 and β_2 , and $q^{vp} = 2\sqrt{k^{vp}} - c^{vp}$ where $k^{vp} = (1 + \sin \phi^{vp})/(1 - \sin \phi^{vp})$ and c^{vp} is a constant, i.e., perfect viscoplasticity. The plastic flow rule is given by:

$$\dot{\epsilon}^p = \begin{cases} \dot{\lambda} \frac{\partial g}{\partial \sigma} & \text{for } f > 0 \\ \mathbf{0}, & \text{for } f \leq 0 \end{cases}, \quad (4)$$

where $\dot{\lambda}$ is the plasticity multiplier and g is a potential flow analogous to f to simulate the volume dilatation during the evolution of plastic deformations. However, for this analysis, was used associated plasticity, i.e., $g = f$. The plastic multiplier is obtained through the consistency condition $\dot{f} = 0$. Numerical details of this implementation can be found in [18]. For viscoplastic flow rule we have,

$$\dot{\epsilon}^{vp} = \dot{\lambda}^{vp} \frac{\partial f^{vp}}{\partial \sigma} \quad (5)$$

In contrast to the plastic multiplier, the viscoplastic multiplier $\dot{\lambda}^{vp}$ is independent of a consistency condition. As a result, its expression is explicit. For this study, we utilize the Perzyna model as follows:

$$\dot{\lambda}^{vp} = \frac{\Phi(\sigma, q^{vp})}{\eta} \quad \text{and} \quad \Phi = \left\langle \frac{f^{vp}(\sigma, q^{vp})}{f_0} \right\rangle^n, \quad (6)$$

where Φ is the overstress function, η is the dynamic viscosity constant, n is the dimensionless parameter that gives the form of the power law, f_0 a parameter conveniently adopted and $\langle * \rangle$ is the McCauley function which is 0 when $* < 0$, i.e. viscoplastic flow will only occur when the overstress function is positive.

In this coupled model, when $\phi = \phi^{vp}$, cohesion entirely controls the evolution of local mechanical fields. Specifically, when $c \rightarrow \infty$ and $c^{vp} \rightarrow \infty$, the system achieves a purely elastic solution. The solution becomes purely elastoviscoplastic with $c \rightarrow \infty$, while a pure elastoplastic solution emerges with $c^{vp} \rightarrow \infty$. In this study's coupled analysis, we have adopted $c^{vp} < c$, allowing the viscoplastic domain to occur without plasticity. However, in the presence of plasticity, viscous effects become inevitable. Fig. 2 illustrates these domains in principal stress space.

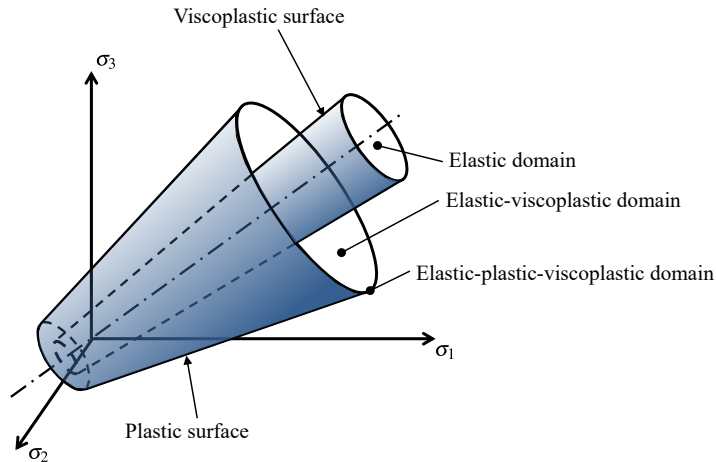


Figure 2: Elastoplastic-viscoplastic domains.

Details of this model, including validations and its application in single tunnel, are in [18]. See [16] for the algorithm details implemented in FORTRAN within the USERMAT subroutine.

4. Constitutive Model of the Lining

We implemented a viscoelastic model in ANSYS using the UPF/USERMAT customization feature [1]. The model simulates concrete creep through a Generalized Kelvin chain, based on Bažant and Prasannan's Solidification Theory

[2; 3], with parameter adjustments performed using the CEB-FIP MC90 formulation. The CEB-FIP MC90 formulation also [5] determines the shrinkage component.

In this model, the constitutive relationship between stress and strain is

$$\dot{\sigma} = \mathbf{D} : \dot{\epsilon}^e = \mathbf{D} : \dot{\epsilon} - \mathbf{D} : \dot{\epsilon}^{sh} - \mathbf{D}^* : \dot{\epsilon}^{cr} \quad (7)$$

where $\dot{\epsilon}^{sh}$ and $\dot{\epsilon}^{cr}$ are the shrinkage and creep strain rate, respectively, while \mathbf{D} and \mathbf{D}^* denote the fourth-order isotropic elastic linear constitutive tensor and modified constitutive tensor that incorporates the aging of the concrete, respectively. Due to the time integration scheme for the Newton-Raphson algorithm, the Eq. (7) is given by:

$$\sigma_{n+1} = \sigma_n + \mathbf{D} : \Delta\epsilon - \mathbf{D} : \Delta\epsilon^{sh} - \mathbf{D}^* : \Delta\epsilon^{cr} \quad (8)$$

in which the increment of shrinkage strain is:

$$\Delta\epsilon^{sh} = \Delta\epsilon_{sh}(t_s)\mathbf{1} \quad (9)$$

where t_s represents the concrete curing time, and $\Delta\epsilon_{sh}$ is the variation of magnitude of the concrete deformation by shrinkage, determined using the expressions of CEB-FIP MC90 [5]. To calculate the increment of creep strain, denoted as $\Delta\epsilon^{cr}$, we use the incremental algorithm developed by Bažant and Prasannan [2; 3], with an adjustment to incorporate CEB-FIP MC90 formulation. This adaptation is possible comparing the creep functions $J(t, t_0)$ of both references. This gives to the following equivalence:

$$E_0 = E_c(t_0), \gamma_c(t - t_0) = \beta_c(t - t_0), \frac{1}{\nu(t)} = \frac{\phi_0}{E_{ci}} \text{ and } \frac{1}{\eta(t)} = 0 \quad (10)$$

in which, according to Bažant and Prasannan [2; 3], E_0 is the modulus of elasticity of the concrete aggregates and microscopic particles of the cement paste, $\gamma_c(t - t_0)$ is the microviscoelastic deformation of the volume fraction of solidified concrete $\nu(t)$, $\eta(t)$ is the apparent macroscopic viscosity and, according to CEB-FIP MC90 [5], $E_c(t_0)$ is the tangent elastic modulus of the concrete at the instant of loading application t_0 , $\beta_c(t - t_0)$ is a coefficient that depends on the loading age $t - t_0$, ϕ_0 is a coefficient that depends on the age of the concrete at the instant of loading application and E_{ci} the tangent elasticity modulus of the concrete at the age of 28 day.

Details of this model, including validations and its application in single tunnel, are in [17]. See [15] for the algorithm details implemented in FORTRAN within the USERMAT subroutine.

5. Spatial and time discretization of the domain

The problem domain Ω consists of a twin deep tunnel with a cross gallery, as shown in Fig. 3.

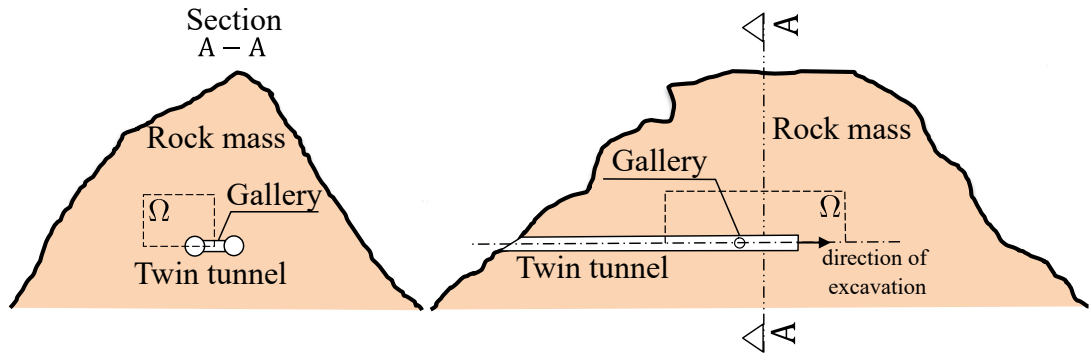


Figure 3: Problem domain

The spatial discretization of the domain Ω corresponds to a mesh with trilinear hexahedral elements (SOLID 185, 8 nodes), except in the gallery region, which uses higher-order tetrahedral elements (SOLID186, 10 nodes). Fig. 4 shows the mesh, geometric parameters, and boundary conditions for the domain problem. We considered front, side,

and bottom symmetry to reduce computational cost. In this discretization, d_1 is the distance between longitudinal tunnel axes, R_i longitudinal tunnel cross-section radius, L_2 total excavated length, d_3 domain height, L_1 length of the unexcavated region, L_3 transversal length of the domain, L_p step length of the excavation process, d_2 position of the gallery along the longitudinal tunnel. In conjunction with boundary pressure p , we apply the initial stress condition $\sigma_0 = -p\mathbf{1}$ at all integration points to simulate the initial state of an undisturbed rock mass.

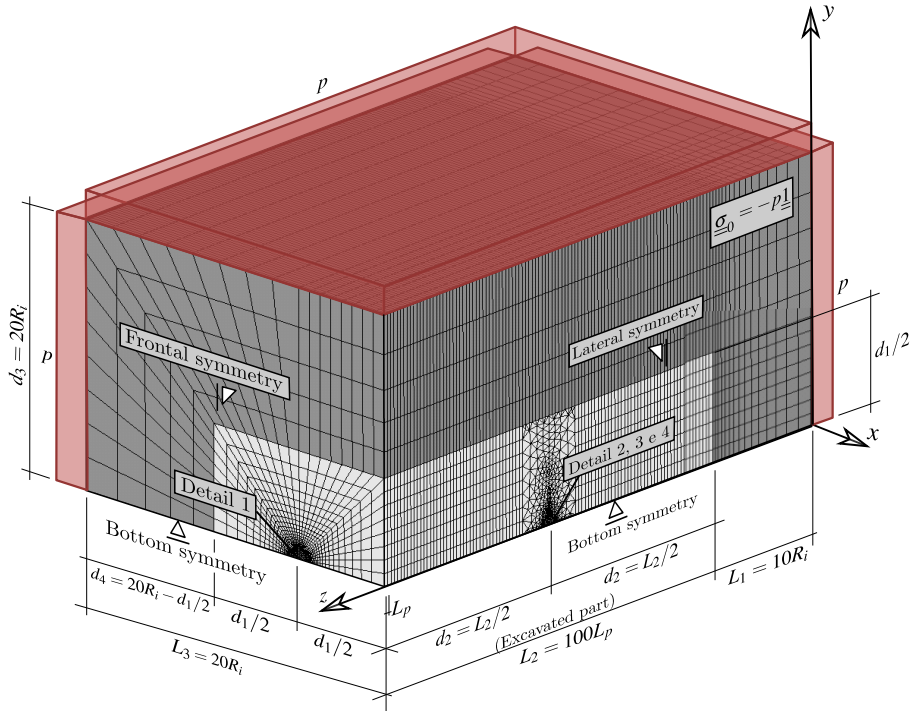


Figure 4: Mesh, dimensions and boundary conditions of the 3D twin tunnel domain

We divided the mesh into two regions: one near the tunnel (light gray), which we refined more, and a region farther away (dark gray), which we increased the aspect ratio to minimize the number of elements in that region. Due to the low deformation gradient away from the tunnel wall, elements in this area can be considerably larger than in other regions. Fig. 5 presents the mesh at the cross-section of the longitudinal tunnel, with e representing the thickness of the lining.

Transverse gallery of twin tunnels

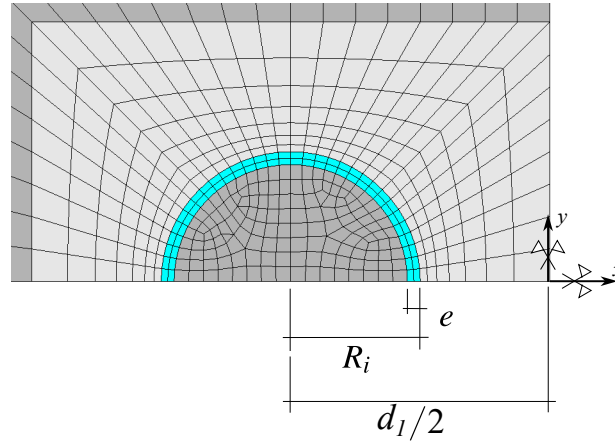


Figure 5: Detail 1 - Mesh in longitudinal tunnel cross-section with spacing $d_1 = 4R_i$

One of the aspects investigated in this work is the influence of the spacing d_1 between longitudinal tunnels of the twin tunnel. Fig. 6 and Fig. 7 illustrate the spatial discretization in the gallery region and its connection with the longitudinal tunnel considering spacings $d_1 = 16R_i$, $8R_i$ and $4R_i$, respectively. We adopt the radius of the gallery as $2/3R_i$, and its lining has the same thickness as the longitudinal tunnel. The dimensions d_5 and d_1 define the size of the transition region comprising tetrahedral elements between the gallery and the rest of the domain. Fig. 8 shows half of this transition region inside the rock mass.

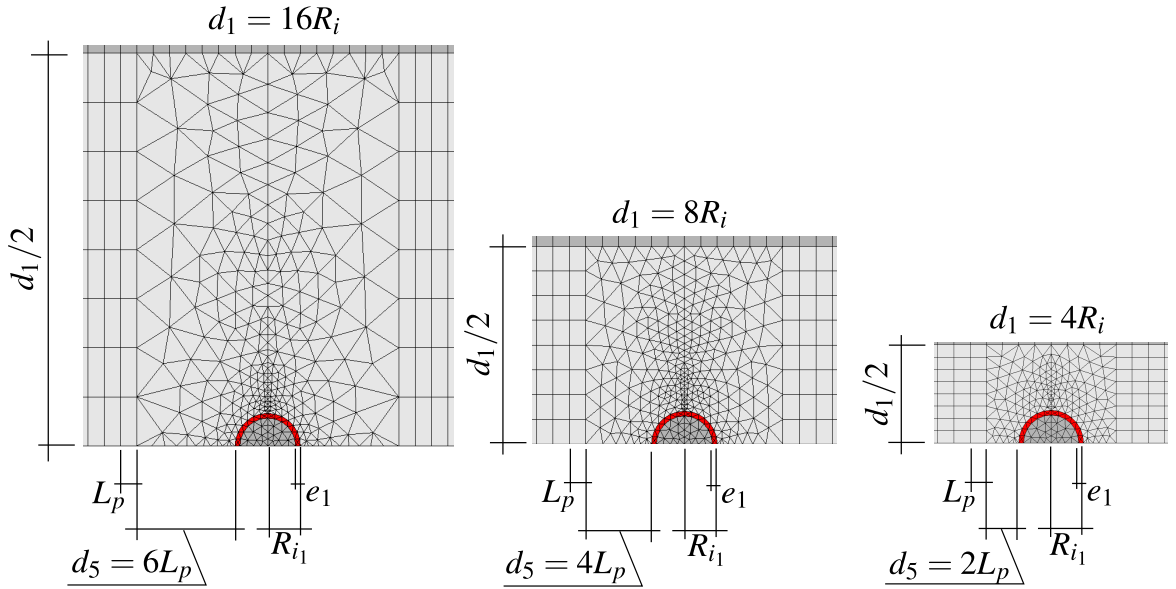


Figure 6: Detail 2 - Side view of the mesh in gallery region with $d_1 = 16R_i$, $d_1 = 8R_i$ and $d_1 = 4R_i$

Transverse gallery of twin tunnels

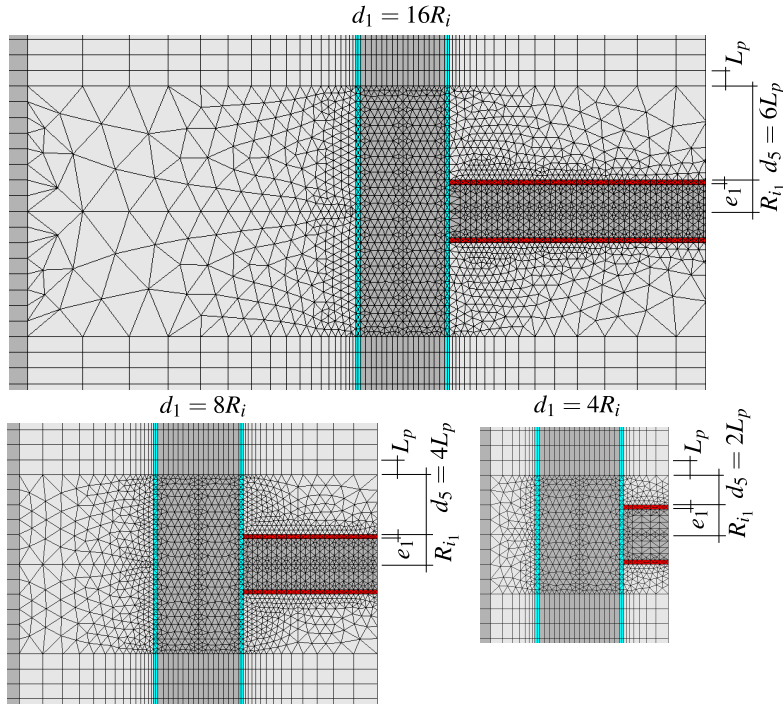


Figure 7: Detail 3 - Bottom view of the mesh in gallery region with $d_1 = 16R_i$, $d_1 = 8R_i$ and $d_1 = 4R_i$

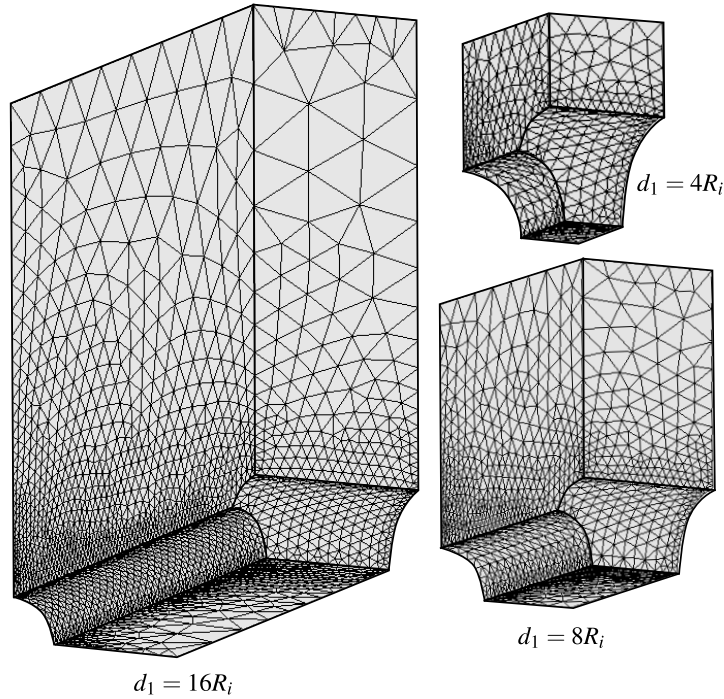


Figure 8: Detail 4 - Isometric view of the portion of the mesh in gallery transition region $d_1 = 16R_i$, $d_1 = 8R_i$ and $d_1 = 4R_i$

Fig. 9 shows the mesh of the lining at the junction of the gallery and the longitudinal tunnel for $d_1 = 4R_i$, $8R_i$, and $16R_i$. One noteworthy characteristic of this mesh is that it confines the tetrahedral elements within the contour of every excavation step.

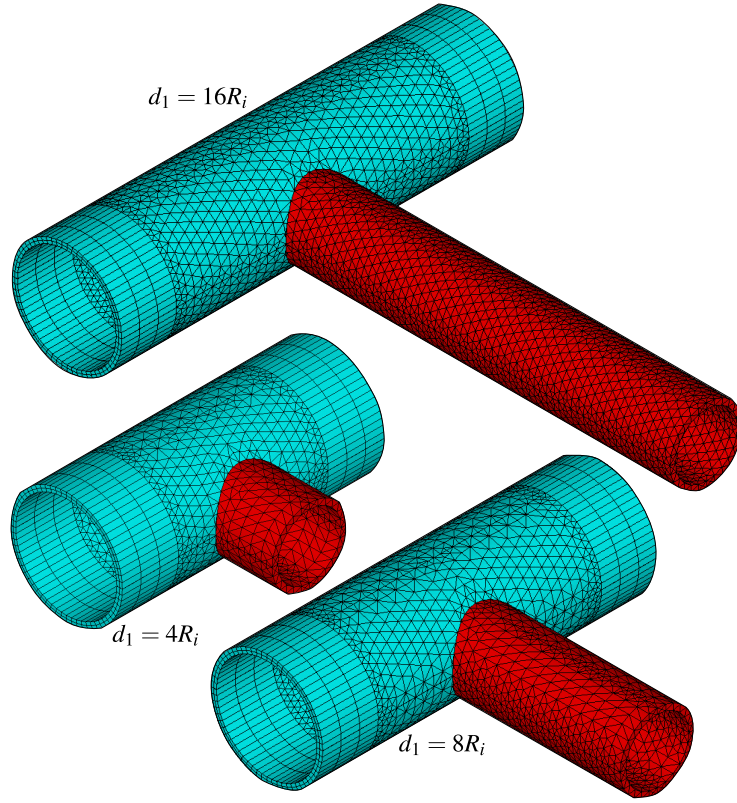


Figure 9: Isometric view of the lining at the intersection for $d_1 = 16R_i$, $d_1 = 8R_i$ and $d_1 = 4R_i$ - expansion of symmetry in the xz plane

The construction process is simulated through the deactivating and activating method, i.e., in each step of excavation, reducing the stiffness of the excavated element (multiply by $1E-8$) and active the lining elements at a distance d_0 from the excavation face (unlined length). With each excavation step, we execute the solution, and time advances based on the expression $t_p = L_p/V_p$, where L_p represents the length of the excavation step, and V_p is the speed of the excavation face. Fig. 10 illustrates a schematic of the excavation process where n_p is the number of excavation steps. In this Figure, n_{pig} represents the number of steps excavated in the longitudinal tunnel that starts gallery excavation. Once reaching this step, we pause the excavation of the longitudinal tunnel, and the gallery excavation begins. In the gallery, L_{p1} is the step length of the gallery excavation, V_{p1} is the speed of the gallery excavation, and d_{01} is the unlined length of the gallery. After completing the gallery excavation, the longitudinal tunnel excavation resumes. These parameters related to the geometry domain, excavation and installation of the lining are shown in Table 1.

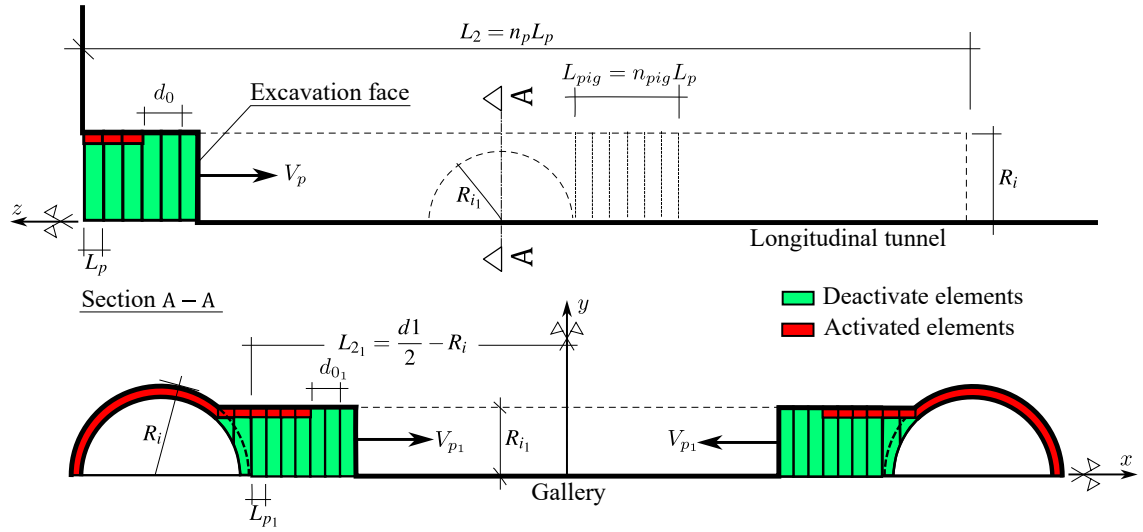


Figure 10: Schematic of the excavation process

Table 1

Parameters related to the geometry of the domain, excavation and installation of the lining

PARAMETERS	SYMBOL	UNIT	VALUES
Longitudinal tunnels			
Longitudinal tunnel cross-section radius	R_i	m	1
Thickness of the lining	e	m	$0.1 R_i$
Step length of the excavation process	L_p	m	$1/3 R_i$
Unlined length	d_0	m	$2 L_p$
Speed of the excavation face	V_p	m/day	12.5
Excavation step time	t_p	day	L_p/V_p
Gallery			
Gallery cross-section radius	R_{i1}	m	$2 L_p$
Thickness of the lining	e_1	m	$0.1 R_i$
Step length of the excavation process ¹	L_{p1}	m	$0.3 R_{i1} \quad 0.3214 R_{i1} \quad 0.3387 R_{i1}$
Unlined length	d_{01}	m	$2 L_{p1}$
Speed of the excavation face	V_{p1}	m/day	12.5
Number of steps that starts gallery excavation	n_{pig}	un	15
Rest of domain			
Distance between longitudinal tunnel axes	d_1	m	$4 R_i \quad 8 R_i \quad 16 R_i$
Length of the unexcavated region	L_1	m	$10 R_i$
Total excavated length	L_2	m	$100 L_p$
Domain height	L_3	m	$20 R_i$

¹ $L_{p1} \approx 1/3 R_{i1}$ in such a way that there are n integer excavation steps in $d_1 - 2 R_i$

During tunnel construction, we determine the initial time increment for solution steps as $0.5t_p$ (for the longitudinal tunnel) and $0.5t_{p1}$ (for the transverse gallery). ANSYS manages the time increment using the bisection method, halving the time step if there is no equilibrium convergence.

After tunnel excavation, in time-dependent constitutive models, time continues to progress to capture long-term viscous effects. In this stage, each time step lasts 100 days, with an initial increment of 50 days. This increase, compared to the excavation time increments, is facilitated by the semi-implicit scheme in the viscoplasticity solution. The explicit scheme, as indicated in [20], requires a smaller time increment to the precision of the solution.

6. Comparison with analytical solutions in twin tunnel

To examine mesh convergence and validate the numerical model, we compared the numerical solution with the elastic and elastoplastic analytical solution in the plane state of deformations for twin tunnels. Guo et al. [12] develop an elastic analytical solution for the stress field around twin circular tunnels with hydrostatic pressure using the complex variable and the superposition principle. The Fig. 11 shows the tangential stress distribution around the tunnel's boundary in this analytical solution with the numerical solution considering $R_i = 4$ m, $E = 500$ MPa, $\nu = 0.23$, $d_1 = 2R_i$, $p = 2.2$ MPa.

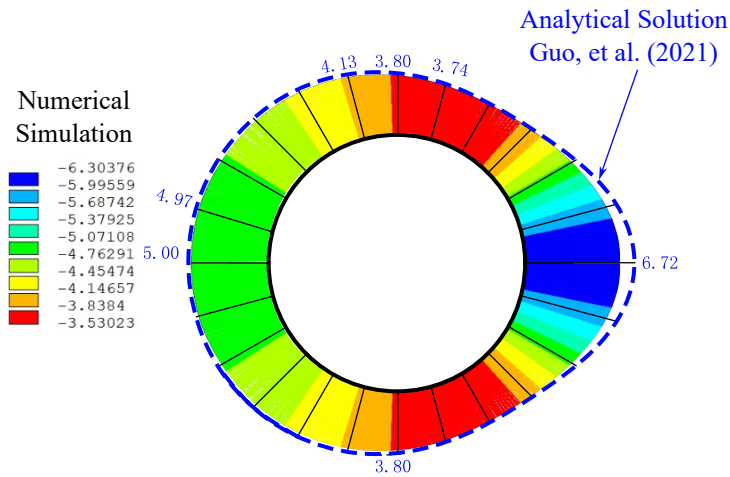


Figure 11: Verification of numerical results of orthoradial stresses with the analytical solution

Ma et. al. [13] developed an analytical solution for a perfectly plastic constitutive model with a Mohr-Coulomb surface. One of the results was the contour of the plastic zone for several conditions. Fig. 12 shows the comparison between the numerical model solution (taken from a section away from the excavation face) and the analytical solution. For these analysis, $R_i = 1$ m, Young's modulus $E = 20$ GPa and Poisson's ratio $\nu = 0.3$.

Transverse gallery of twin tunnels

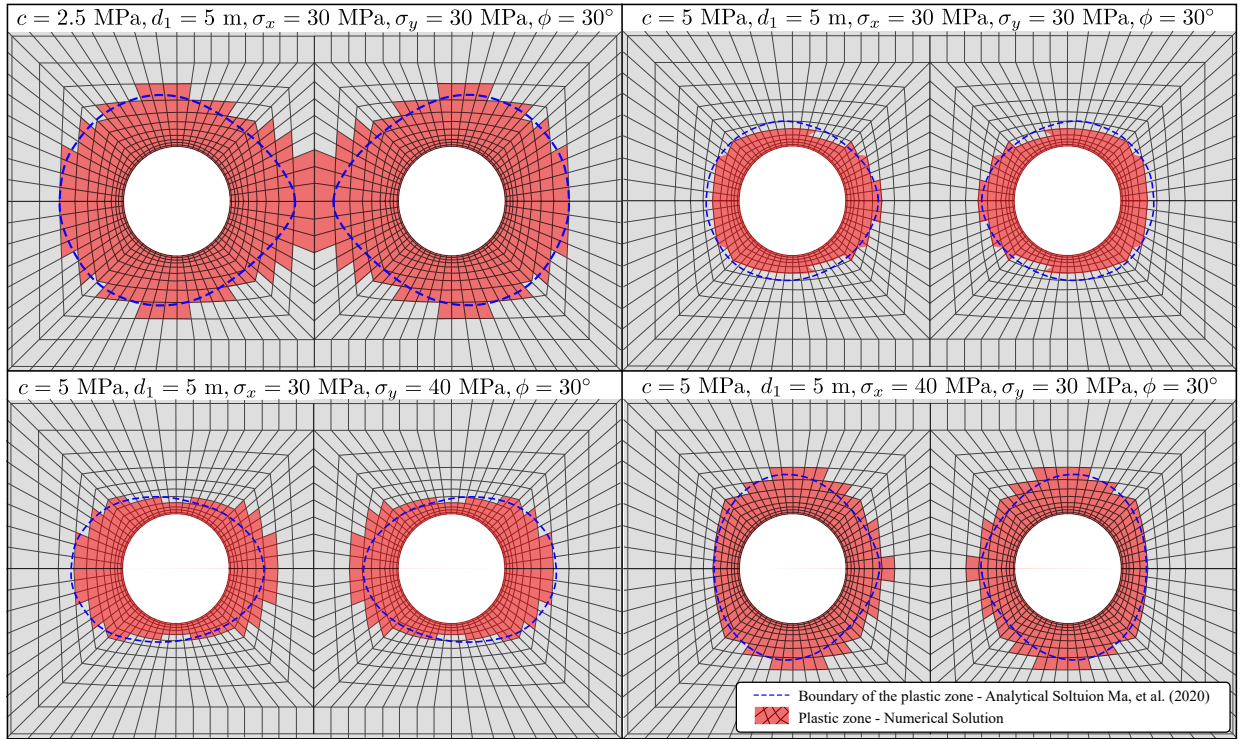


Figure 12: Numerical and analytical comparison of plastic zones

Fig. 13 displays the magnitude of displacements, radial, orthoradial, and z-direction stresses at the element level for the case with $c = 5$ MPa, $d_1 = 5$ m, $\sigma_x = \sigma_y = 30$ MPa. We adopted a case without excavating the gallery to assess the quality of the mesh. The smoothness observed in the solution between the elements indicates satisfactory discretization.

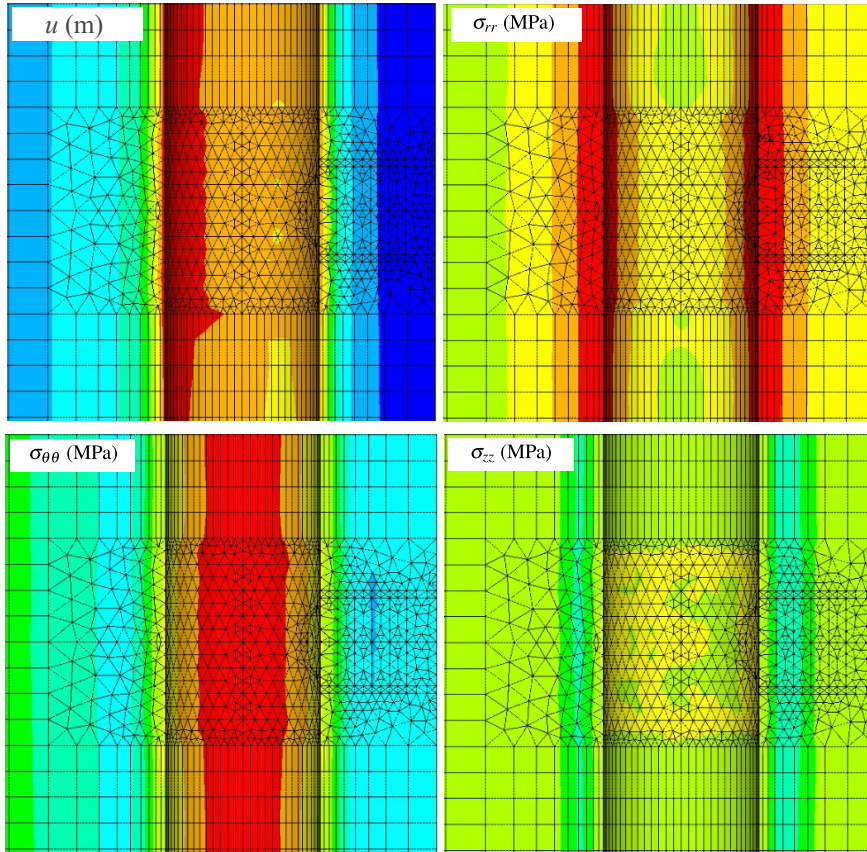


Figure 13: Element solution with $c = 5$ MPa, $d_1 = 5$ m, $\sigma_x = \sigma_y = 30$ MPa

7. Numerical Results and Discussion

To develop the parametric analyses, we utilized the constitutive parameters of the rock mass as outlined in Piepi [14], and for the lining, we employed typical values for ordinary reinforced concrete. These parameters are shown in Table 2. In these analyses, an isotropic initial stress state of 9MPa is considered, and the excavation speed is 12.5m/day [14].

Table 2

Constitutive parameters used in the parametric analysis

PARAMETERS	SYMBOL	UNIT	VALUES
Constitutive model of rock mass			
Young's modulus	E	MPa	1500
Poisson's ratio	ν	adm	0.498
Plastic cohesion	c	MPa	$4\sqrt{3}/2$
Plastic friction angle	ϕ	°	0
Viscoplastic Cohesion	c_{vp}	MPa	$2\sqrt{3}/2$
Viscoplastic friction angle	ϕ_{vp}	°	ϕ
Power law parameter	n	adm	1
Reference parameter	f_0	MPa	1
Viscosity coefficient	η	day	40000
Constitutive model of lining			
Compressive strength	f_{ck}	MPa	20
Young's modulus at 28 days	E_{c28}	MPa	30303
Poisson's ratio	ν	adm	0.3
Coefficient which depends on the type of cement	s	adm	0.2
Relative humidity of ambient environment	RH	%	70
Fictitious thickness (longitudinal tunnel)	h_f	cm	0.2111
Fictitious thickness (transverse gallery)	h_f	cm	0.2176
Drying time of the concrete	t_s	days	7
Coefficient in shrinkage which depends on the type of cement	β_{sc}	adm	8
Temperature	T	°C	20°
Age of concrete at loading	t_0	days	1

In presenting the results, U_{eq} denotes the equilibrium convergence value at the convergence profile outside the region of influence of the excavation face and the gallery. When the gallery is present, the highest convergence value, U_{peak} is highlighted at the gallery position. In addition, it is necessary to highlight some important points:

- **Observation 1:** All the results presented in the following analyses pertain to the point located at the top of the tunnel section (crown), and we will monitor its convergence throughout the excavation process. Fig. 14 presents this point. Likewise, we will only analyze the convergence of the point located at the crown of the gallery.
- **Observation 2:** Under material isotropy and initial stress state, the symmetry of the tunnel wall is preserved throughout the excavation process. Thus, the deformed tunnel wall remains circular. On the other hand, one of the effects of the mutual interaction induced by the proximity of the tunnels is the loss of symmetry of the deformed tunnel wall, as illustrated in Fig. 14. In this context, the point chosen to follow the convergences (on the crown) is not representative of the entire deformation of the tunnel wall.
- **Observation 3:** Referring to the material properties shown in Table 2, the value adopted for plastic cohesion (c) is higher than the value for viscoplastic cohesion (c_{vp}): $c > c_{vp}$. This implies that in the regime of irreversible deformations, the viscoplasticity of the material will be activated first. Throughout the excavation process, viscoplastic deformations will appear without plasticization of the massif. The generic configurations of the deformation zones of the massif throughout the excavation process are illustrated in Fig. 15.

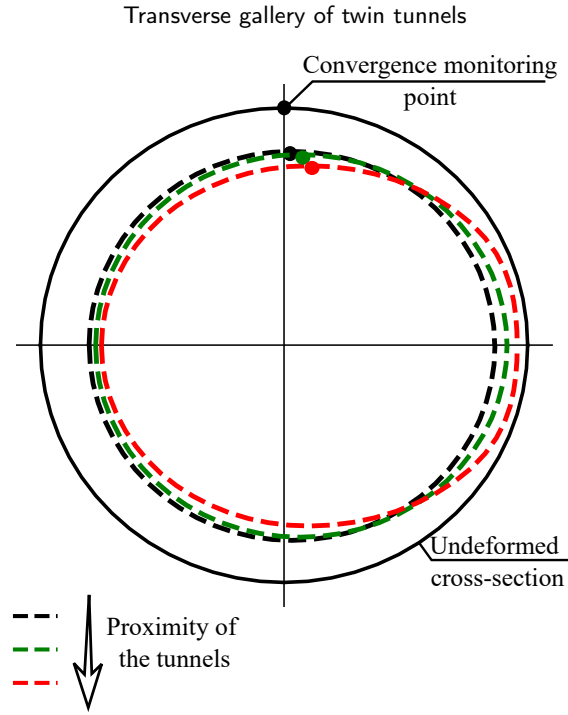


Figure 14: Monitoring point and ovalization effect

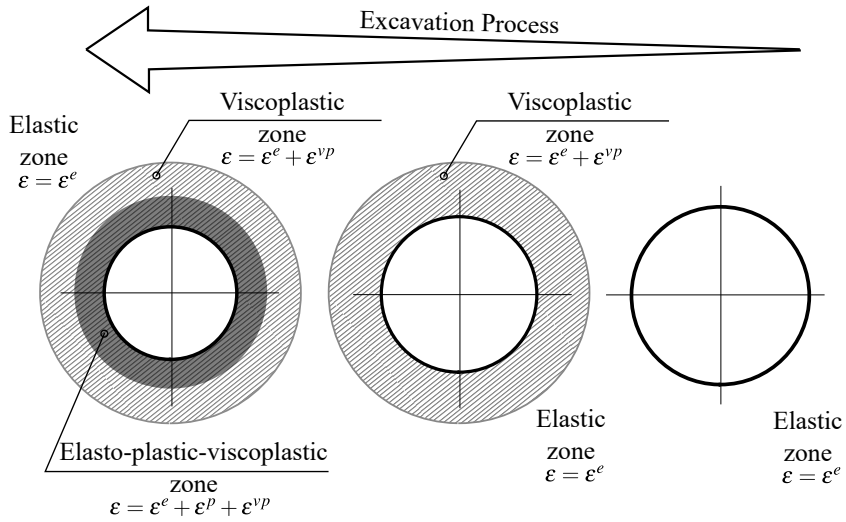


Figure 15: Configurations for the zones with irreversible deformations in the rock mass

Table 3 presents the abbreviation to read the title and legend of the results.

Table 3

Abbreviation to the title and legend of the results

DESCRIPTION	ABBREVIATION
Elastic rock mass	E
Elastoplastic rock mass	EP
Elastoviscoplastic rock mass	VP
Elasto-Plastic-Viscoplastic rock mass	EPVP
Elastic lining	EL
Viscoelastic lining	VEL
Long-term	LT
Final excavation (Short-term)	ST
With Gallery	WG
Not Gallery	NG

Figures X, Y, and Z show the convergence profiles of the twin tunnels with gallery for all the constitutive models of the massif (E - blue, EP - yellow, VP - pink, EPVP - red) and the lining (EL and VEL) in the short term (full line) and the long term (dashed line), for $d_1 = 4R_i$, $8R_i$ and $16R_i$ respectively.

WGSTLT-D14RE WGSTLT-D18RE WGSTLT-D116RE

In all these results, there is an equivalence between the convergence profiles of the E-EL model (blue dashed line) and the VP-EL in the ST (magenta dashed line), probably due to the high excavation speed. The rapid process of excavation and installation of the lining limits the time for the viscous effects to manifest themselves, also taking into account the restriction imposed by the stiffness of the lining.

In the ST (short term), the EPVP-EL model (green solid line) is equivalent to the EP-EL (yellow dashed line) because, although plasticization around the section has already occurred due to excavation, the viscous effects have not yet evolved considerably due to the short time variation between the start of excavation and the end of the excavation process. After the long term, convergence occurs (green dashed line). However, when the rheological effect of the lining is present, the profile continues to evolve considerably over the long term EPVP-VEL (red dashed line).

7.1. Influência do afastamento entre os túneis

7.2. A influência da rigidez do revestimento

7.3. A influência da presença da galeria no túnel longitudinal

7.4. Abrangência da região de influência da galeria

7.5. A influência dos modelos que envolve efeitos diferidos

8. Conclusions

As principais conclusões do estudo podem ser apresentadas numa breve secção de Conclusões, que pode ser autónoma ou constituir uma subsecção de uma secção de Discussão ou de Resultados e Discussão.

References

- ANSYS, 2013. ANSYS Programmer's Reference; release 15.0. Canonsburg, Pennsylvania.
- Bažant, Z.P., Prasannan, S., 1989a. Solidification theory for concrete creep. i: Formulation. *Journal of engineering mechanics* 115, 1691–1703. doi:[https://doi.org/10.1061/\(ASCE\)0733-9399\(1989\)115:8\(1691\)](https://doi.org/10.1061/(ASCE)0733-9399(1989)115:8(1691)).
- Bažant, Z.P., Prasannan, S., 1989b. Solidification theory for concrete creep. ii: Verification and application. *Journal of engineering mechanics* 115, 1704–1725. doi:[https://doi.org/10.1061/\(ASCE\)0733-9399\(1989\)115:8\(1704\)](https://doi.org/10.1061/(ASCE)0733-9399(1989)115:8(1704)).
- Bernaud, D., 1991. Tunnels profonds dans les milieux viscoplastiques: approches expérimentale et numérique. Ph.D. thesis. Ecole Nationale des Ponts et Chaussées. Paris, French.
- CEB-FIP, 1993. CEB-FIP model code 1990: Design code. Comité Euro International du Béton and Fédération Internationale de la Précontrainte (CEB-FIP).
- Chen, F., Lin, L.b., Li, D., 2019. Analytic solutions for twin tunneling at great depth considering liner installation and mutual interaction between geomaterial and liners. *Applied Mathematical Modelling* 73. doi:[10.1016/j.apm.2019.04.026](https://doi.org/10.1016/j.apm.2019.04.026).
- Chortis, F., Kavvas, M., 2021a. Three-dimensional numerical analyses of perpendicular tunnel intersections. *Geotechnical and Geological Engineering* 39, 1771–1793.

- Chortis, F., Kavvadas, M., 2021b. Three-dimensional numerical investigation of the interaction between twin tunnels. *Geotechnical and Geological Engineering* 39, 5559–5585. doi:<https://doi.org/10.1007/s10706-021-01845-5>.
- Chortis, F., Kavvadas, M., 2023a. 3d numerical investigation of the axial forces acting on tunnel junctions constructed in fractured/weathered to very blocky rockmass, in: *Expanding Underground-Knowledge and Passion to Make a Positive Impact on the World*. CRC Press, pp. 1574–1582.
- Chortis, F., Kavvadas, M., 2023b. 3d numerical investigation of the bending moments acting on tunnel junctions constructed in fractured/weathered to very blocky rockmass, in: *Expanding Underground-Knowledge and Passion to Make a Positive Impact on the World*. CRC Press, pp. 1583–1591.
- Fortsakis, P., Bekri, E., Prountzopoulos, G., Marinos, P., 2012. Numerical analysis of twin tunnels interaction, in: *Proc. 1st Eastern European Tunnelling Conference*, pp. 1–8.
- Guo, Z., Liu, X., Zhu, Z., 2021. An elastic solution for twin circular tunnels' stress in hydrostatic stress field. *Geotechnical and Geological Engineering* 39, 1–11. doi:[10.1007/s10706-021-01756-5](https://doi.org/10.1007/s10706-021-01756-5).
- Ma, Y., Lu, A., Zeng, X., Cai, H., 2020. Analytical solution for determining the plastic zones around twin circular tunnels excavated at great depth. *International Journal of Rock Mechanics and Mining Sciences* 136, 104475. doi:<https://doi.org/10.1016/j.ijrmms.2020.104475>.
- Piepi, G.T., 1995. Comportement viscoplastique avec rupture des argiles raides. Applications aux ouvrages souterrains. Ph.D. thesis. Ecole Nationale des Ponts et Chaussées. Paris, French.
- Quevedo, F.P.M., 2017. Comportamento a longo prazo de túneis profundos revestidos com concreto: modelo em elementos finitos. M.S. thesis. Federal University of Rio Grande do Sul. Porto Alegre, Brazil.
- Quevedo, F.P.M., 2021. Análise computacional das deformações em túneis profundos considerando o acoplamento plasticidade-viscoplasticidade.
- Quevedo, F.P.M., Bernaud, D., Campos Filho, A., 2022a. Numerical analysis of deep tunnels in viscoplastic rock mass considering the creep and shrinkage of the concrete lining. *International Journal of Geomechanics* 22. doi:[10.1061/\(ASCE\)GM.1943-5622.0002282](https://doi.org/10.1061/(ASCE)GM.1943-5622.0002282).
- Quevedo, F.P.M., Bernaud, D., S., M., 2022b. Numerical integration scheme for coupled elastoplastic–viscoplastic constitutive law for tunnels. *International Journal of Geomechanics* 22. doi:[10.1061/\(ASCE\)GM.1943-5622.0002512](https://doi.org/10.1061/(ASCE)GM.1943-5622.0002512).
- Spyridis, P., Bergmeister, K., 2015. Analysis of lateral openings in tunnel linings. *Tunnelling and Underground Space Technology* 50, 376–395. doi:[10.1016/j.tust.2015.08.005](https://doi.org/10.1016/j.tust.2015.08.005).
- Zienkiewicz, O., Corneau, I., 1974. Visco-plasticity—plasticity and creep in elastic solids—a unified numerical solution approach. *International Journal for Numerical Methods in Engineering* 8, 821–845. doi:<https://doi.org/10.1002/nme.v8:4>.